Observation of inversion, hysteresis, and collapse of spin in optically trapped polariton condensates

Yago del Valle-Inclan Redondo,[1,*] Helgi Sigurdsson,[2] Hamid Ohadi,[1,3,†] Ivan A. Shelykh,[2,4] Yuri G. Rubo,[5] Zacharias Hatzopoulos,[6] Pavlos G. Savvidis,[4,6,7] and Jeremy J. Baumberg[1,‡]

[1]*NanoPhotonics Centre, Department of Physics, Cavendish Laboratory, University of Cambridge, Cambridge CB3 0HE, England, United Kingdom*

[2]*Science Institute, University of Iceland, Dunhagi-3, IS-107 Reykjavik, Iceland*

[3]*School of Physics and Astronomy, University of Saint Andrews, Saint Andrews KY16 9SS, Scotland, United Kingdom*

[4]*Department of Nanophotonics and Metamaterials, ITMO University, Saint Petersburg 197101, Russia*

[5]*Instituto de Energías Renovables, Universidad Nacional Autónoma de México, Temixco, Morelos 62580, Mexico*

[6]*Microelectronics Research Group, IESL-FORTH, Institute of Electronic Structure and Laser, 71110 Heraklion, Greece*

[7]*Department of Materials Science and Technology, University of Crete, 70013 Crete, Greece*

(Received 12 December 2018; revised manuscript received 22 February 2019; published 25 April 2019)

The spin and intensity of optically trapped polariton condensates are studied under steady-state elliptically polarized nonresonant pumping. Three distinct effects are observed: (1) spin inversion where condensation occurs in the opposite handedness from the pump, (2) spin and intensity hysteresis as the pump power is scanned, and (3) a sharp "spin collapse" transition in the condensate spin as a function of the pump ellipticity. We show these effects are strongly dependent on trap size and sample position and are linked to small counterintuitive energy differences between the condensate spin components. Our results, which fail to be fully described within the commonly used nonlinear equations for polariton condensates, show that a more accurate microscopic picture is needed to unify these phenomena in a two-dimensional condensate theory.

DOI: 10.1103/PhysRevB.99.165311

I. INTRODUCTION

Bistability, the existence of two or more stable states for the same parameters of a system, is one of the hallmarks of nonlinear systems [1], and is ubiquitous in the physics of resonantly driven $\chi^{(3)}$-nonlinear optical elements [2]. Microcavity exciton polaritons, the light-matter quasiparticles arising from the strong coupling of quantum well excitons and microcavity photons, present bistability at low optical powers thanks to their strong nonlinearities [3]. The polarization dependence of the nonlinearities causes polarization multistability [4,5], which can be used for the creation of spin memories [6], logic gates [7,8], or switches [9]. However, resonant optical injection is relatively difficult to both implement and practically scale, due to the narrow linewidth of the polariton mode and backscatter destabilization of the laser.

Suitable alternatives have been demonstrated for incoherently pumped polaritons using applied external electric fields, which can cause bistability due to density-dependent lifetimes of electron-hole tunneling [10,11], or through Pockels-induced birefringence [12]. Theoretical schemes have been proposed to induce polariton bistability through modulational instability [13], through strongly saturated absorption [14], or between condensate wave functions of different parity [15].

A typical way of incoherently pumping polaritons is via optical nonresonant excitation, where a hot reservoir of excitons is created from which polaritons can spontaneously develop macroscopic coherence and form a polariton condensate [16], with similar properties to atomic Bose-Einstein condensates [17,18]. The nonlinear interaction between the polariton condensate and its nonresonant exciton cloud can be used to control the condensation landscape for polaritons [19–21], and create optically trapped condensates (Fig. 1) [22–24]. These trapped condensates can spontaneously break the parity symmetry and develop circular polarization (spin) under linearly polarized pumping, stochastically forming in a spin-up or spin-down state randomly when turned on [25].

Here the spin properties of optically trapped polariton condensates under nonresonant pumping with different pump polarization ellipticities are studied. We report on two distinct and unusual effects: spin inversion, which forms condensates with elliptical polarization (spin) of the opposite handedness to that of the nonresonant pump, and spin/intensity bistability with pump power. While such effects were recently reported [26,27], both were attributed to an interplay of linear polarization splitting and spin-asymmetric reservoir nonlinearities within a zero-dimensional model [28]. Studying the dependence of these effects on pump polarization ellipticity and trap size reveals that these two phenomena (1) are strongly trap-size dependent, (2) can only be observed within a certain range of pump ellipticity, (3) can be observed independently from each other, indicating they arise from different physical processes, and (4) are position dependent. A previously unreported sharp transition in the condensate spin as the pump polarization crosses a critical threshold is seen. Conventional mean field models provide only partial agreement with these results.

*ybd20@cam.ac.uk
†ho35@st-andrews.ac.uk
‡jjb12@cam.ac.uk

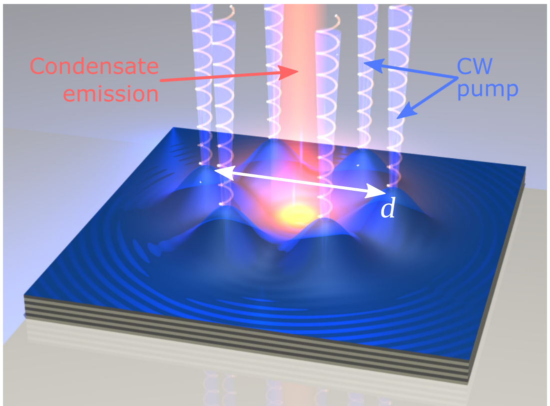

FIG. 1. Nonresonant optical trapping of polariton condensates. The six pump spots create exciton clouds that blueshift the polariton energy and create a trapping potential inside which condensation develops. The trap size (d) is given by the diameter (white arrow).

The rest of this paper is organized as follows. Sample description and experimental methods are covered in the "Experimental procedure" subsection of the Introduction. In Sec. II, the experimental evidence for polarization/intensity bistability and hysteresis is provided. The dependence of this bistability on trap size and sample position is investigated in Sec. III, demonstrating the need for considering spatial degrees of freedom and spatial sample disorder in the description of these condensates. In Sec. IV, the energy and spatial distribution of the condensate is measured, showing that condensation always occurs in the trap's ground state but that there are tiny and counterintuitive energy differences (15 μeV) between the circular polarizations. Numerical simulations based on current models are shown in Sec. V, both from a simplified zero-dimensional model and from full two-dimensional (2D) simulations, showing only partial agreement with the experimental results. Finally, Sec. VI explores possible extensions to these models.

Experimental procedure

A $5\lambda/2$ GaAs microcavity is used, with a quality factor $>$16000, detuned to between -2 and -3 meV, and with 9-meV Rabi splitting (details in Ref. [29]). Condensates are created using a single-mode continuous-wave Ti:sapphire laser (750 nm), chopped into 10-μs pulses with an acousto-optic modulator. A variable-angle IR broadband quarter waveplate is used to control the degree of circular polarization of the laser (referred to from now on as "pump spin" S_p).

A spatial light modulator and an iterative Fourier-transform algorithm [30] are used to shape the beam into six diffraction-limited spots ($\sim$1 μm FWHM), arranged in a hexagon forming a trap with diameter d = 11-14μm (Fig. 1). A 0.4NA microscope objective focuses the laser and collects photoluminescence from the sample, held at 4 K inside a cryostat. This emission is spectrally filtered, polarization resolved, and imaged.

In Secs. II and III the pump power is scanned and the laser pulses used are triangular (linearly increasing and then decreasing the power over time) and the condensate is imaged on a streak camera in single-shot mode. This averages over spatial dimensions but allows single-shot power series and hysteretic effects to be studied. The presented results are for 10-μs triangular pulses, but qualitatively similar results are also obtained with pulses one order of magnitude longer and shorter.

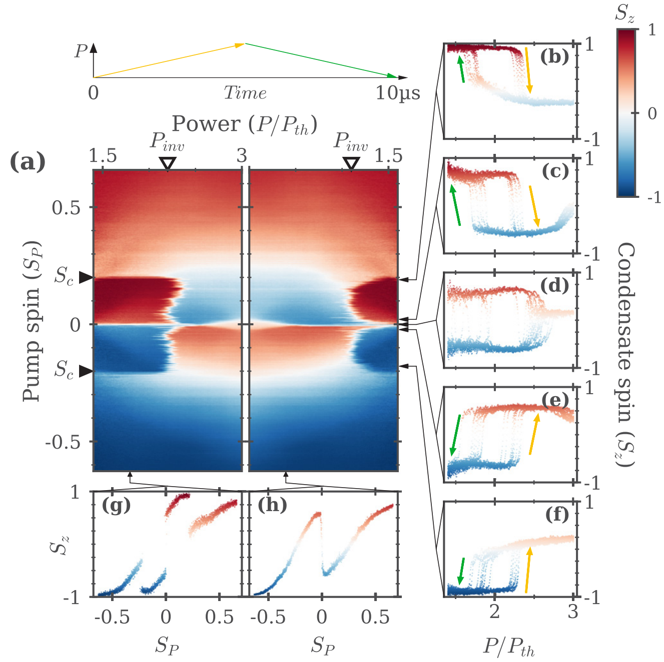

FIG. 2. Spin inversion and hysteresis for a $d = 12.5$-μm trap. (a) Average spin over ten condensate realizations, as a function of pump power and pump spin, while power ramps up and down over 10 μs. (b)–(f) Spin of ten different condensate realizations vs pump power for (b) $S_P = 0.19$, (c) 0.02, (d) 0, (e) -0.02, and (f) -0.18. (g), (h) Spin of ten different condensate realizations vs pump spin for (g) $P = 1.8P_{\rm th}$ and (h) $2.6P_{\rm th}$.

Square laser pulses ($\sim$50-ns turn-on, 5 μs long) with variable power are used in Sec. IV. Single-shot spatial profiles are measured on a CCD, while the energy is measured using a 60-μeV resolution spectrometer and fitting the resulting peaks with a Lorentzian function, with a fitting error $\sim$1–5 μeV. Given typical polariton lifetimes of 10 ps and excitonic lifetimes of 1 ns, the system dynamics are expected to adiabatically follow the pulse power for both Secs. II and III and Sec. IV.

II. HYSTERESIS AND SPIN INVERSION

Since the pumping is tuned far above the polariton emission line ($>$100 meV), the polarization of the exciton cloud below threshold is always very small ($<$5%). This is due to energy relaxation of polaritons by inelastic scattering, which almost completely randomizes the polarization. Above the condensation threshold, however, the condensate spin (S_z) is strongly dependent on the polarization of the nonresonant pump (S_p). Even a very small degree of ellipticity in the pump polarization ($S_P < 2\%$) can lead to strongly spin-polarized condensates [Figs. 2(c) and 2(e)].

For sufficiently large pump ellipticities [$S_P > |S_c|$, filled arrowhead Fig. 2(a)], the condensate always forms in a spin-polarized state of the *same* sign as that of the pumping,

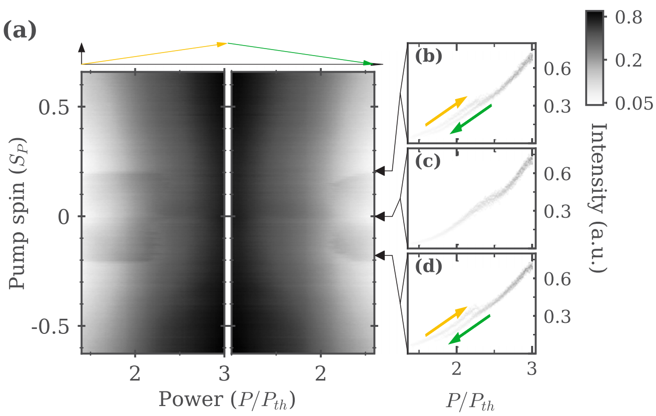

FIG. 3. Intensity hysteresis. (a) Average intensity (log scale) over ten condensates, as a function of pump power and pump spin, while power is ramped up and ramped down. (b)–(d) Intensity of ten different condensates vs pump power for (b) $S_P = 0.21$, (c) 0.0, and (d) -0.18.

independent of pump power. For smaller pump ellipticities, however, the condensate spin is of the same sign as the pump only below a certain power [$P < P_{\text{inv}}$, empty arrowhead in Fig. 2(a)]. Above this threshold, the condensate spin is *opposite* to that of the pumping. This reversal is hysteretic and the threshold power depends on whether the power is being ramped up or down [Figs. 2(b), 2(c), 2(e), and 2(f)]. Both the hysteresis width and degree of circular polarization of the two bistable states depend on this pump spin.

In addition to this condensate spin inversion with power, at low pump powers ($P < P_{\text{inv}}$) there is an additional "spin collapse" transition of the condensate spin as a function of pump spin [marked by S_c in Fig. 2(a)]. The magnitude of the condensate spin is very high ($S_z > 80\%$) if the pump polarization ellipticity is below a critical value [$|S_c| = 0.2$ in Fig. 2(a)]. Hence, at low powers, there are three sharp transitions of the condensate spin versus pump spin [Fig. 2(g)], while at high pump powers there is only one sharp transition when the sign of the pump handedness changes [Fig. 2(h)].

Both the spin inversion (P_{inv}) and the spin collapse (S_c) are accompanied by changes in the condensate intensity (Fig. 3). Just below either of these thresholds (P_{inv} or S_c), the condensate intensity is fractionally higher than above the thresholds [Fig. 3(a)], and displays hysteresis with pump power [Figs. 3(b) and 3(d)].

We note that in the limiting case of a linearly polarized pump [Figs. 2(d) and 3(c)] the main results of our previous works are reproduced. First, the condensate stochastically forms in either a spin-up or a spin-down state with equal probability [25]. Second, once the condensate is formed, noise can induce spin flips between the two spin states before they collapse into a linearly polarized state at higher powers [31]. This collapse to a linearly polarized state can also be seen at high powers for situations with slightly elliptical pumping [Fig. 2(c)].

III. TRAP SIZE AND POSITION DEPENDENCE

The observed spin inversion and hysteresis have strong dependencies on the optical trap size (d in Fig. 1). The two critical thresholds P_{inv} and S_c below which the condensate is brighter and strongly polarized are not observed for all trap sizes. Instead, the regions of brighter emission and stronger polarization (U), as well as the spin-inverted regions (*inv*), have more complicated boundaries in the P-S_P plane (Fig. 4), which radically shift even for diameter changes of $<10\%$.

For smaller trap sizes [Fig. 4(a)], the bright regions U exist for all values of pump spin and down to the lowest pump power at the condensation threshold (P_{th}). These regions display hysteresis in both spin (top row) and intensity (bottom row) with pump power, and it is possible to observe hysteresis without spin inversion [black arrow Fig. 4(a)]. As the trap size increases, the U regions shrink: they no longer occur for all values of pump spin, nor do they occur down to the condensation threshold [Fig. 4(b)]. This shrinking continues as the trap size is increased, until the U manifold becomes so unstable

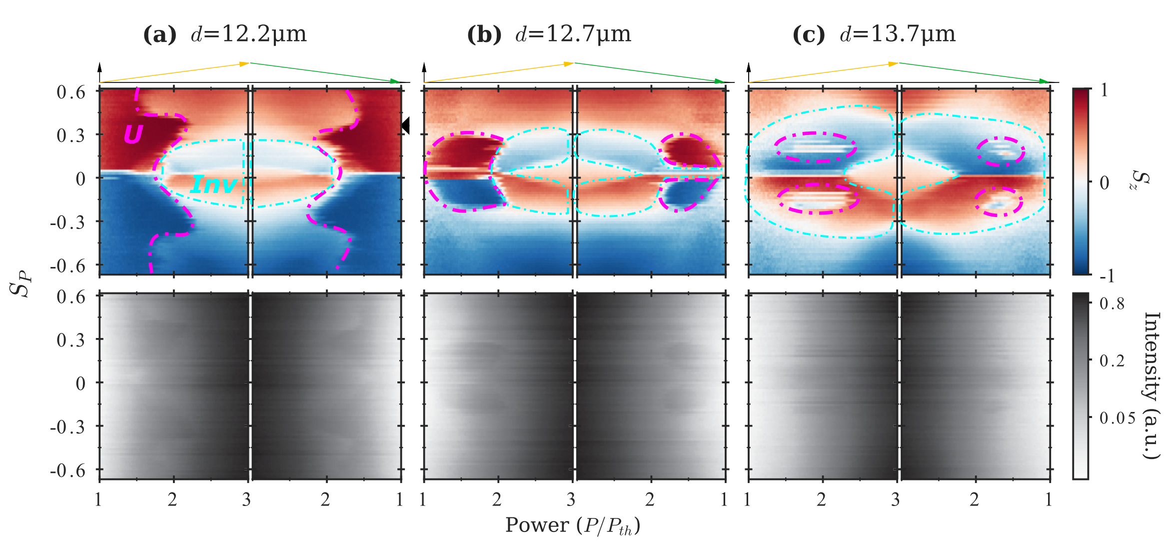

FIG. 4. Average condensate spin and intensity, as functions of pump spin and power, for three different trap sizes. Dashed lines highlight the bright hysteretic regions U (magenta) and spin-inverted regions *inv* (cyan).

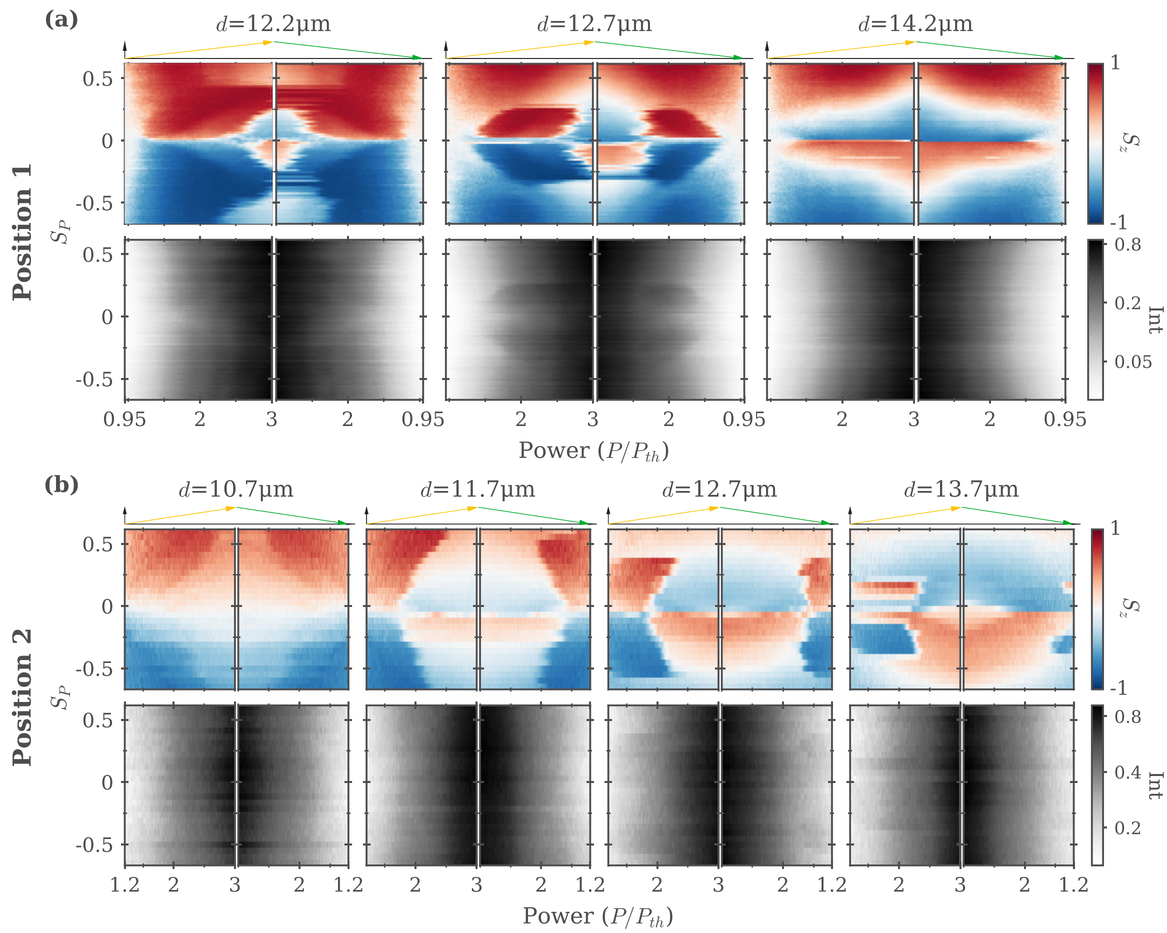

FIG. 5. Average condensate spin and intensity, as functions of pump spin and power, for different trap sizes, at two different positions in (a) and (b). The slight asymmetry along the pump spin axis is due to sample birefringence.

that only few condensate realisations explore it, leading to unpolarized regions in the average polarization [Fig. 4(c)]. For sufficiently large trap sizes, U disappears completely.

While the bright regions shrink and disappear, the regions where spin inversion occurs grow with increasing trap size [*inv* in Fig. 4(a)]. While for the smaller trap sizes spin inversion only occurs at powers above the condensation threshold, for large traps the spin inversion can occur even at condensation [Fig. 4(c)], while also being observed for a larger range of pump ellipticities (S_P). In contrast with the bright regions U, the spin-inverted regions never show any hysteresis with pump power.

The specific shapes of the bright and the spin-inverted regions, and their dependence on trap size, differ with sample position (Fig. 5). For some sample positions and trap sizes, much higher powers are needed to observe spin inversion [Fig. 5(a)]. In other positions, the smallest trap sizes do not present any spin inversion [$d = 10.7\mu$m in Fig. 5(b)].

The length scale over which these changes occur is relatively small: moving the sample a few tens of micrometers can lead to significant variation in the specific power, pump spin, and trap size dependences. This indicates that subtle local sample properties are playing an important role in controlling spin inversion and/or hysteresis, even though there is not *any* measurable disorder in the sample photoluminescence intensity or energy over these length scales. Despite this variability with sample position, the main qualitative dependence on trap size remains. For the smallest traps, the strongly polarized bright hysteretic regions are largest and spin inversion can even disappear. As the trap size is increased, the hysteretic regions shrink and only appear for a finite range of pump powers and pump spin magnitudes, while the spin-inversion region grows. Finally, for the largest traps, the bright hysteretic regions disappear completely and only spin inversion remains.

IV. SPATIAL PROFILES AND CONDENSATE ENERGY

An important factor that changes the behavior of optically trapped polariton condensates is the occupation of multiple trap modes [32]. Even small occupations of higher-order modes can significantly affect the condensation dynamics and complicate the interpretation of experimental results. However, no evidence of these in the condensate spatial or energy profiles is seen.

Despite using square laser pulses instead of ramped pulses (Sec. I), the same qualitative trends of the spin-inverted and bright regions as a function of trap size are observed [Fig. 6(b)]. The bright, hysteretic regions are largest for smaller traps, and shrink as the trap size is increased.

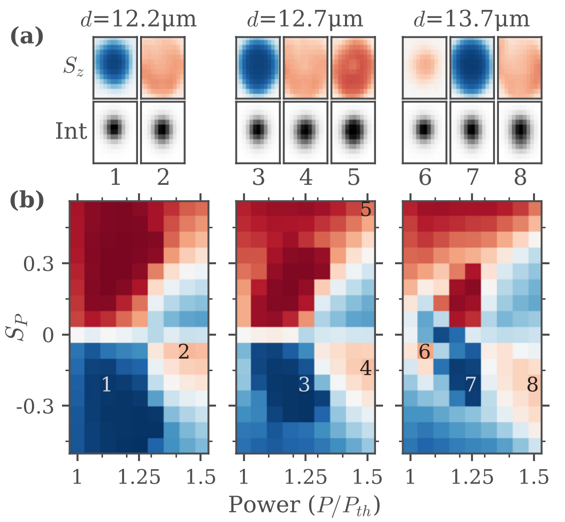

FIG. 6. (a) Spatial profiles of the condensate spin and intensity and (b) average spin as a function of pump spin for these three different trap sizes. Each of the panels in (a) correspond to a single pixel in (b).

Although the spin and intensity of the condensate depend strongly on the spatial confinement, the shape of the condensate itself, both in spin and intensity, remains unchanged for all pump powers and pump spins. The similarity between Figs. 4 and 6 supports the fact that the dynamics are adiabatic, even with square pulses. Given that the exposure time is much longer than the rise and fall time, the measured spatial and energy profiles are a good approximation to their steady-state values.

Spin and intensity profiles do not increase in spatial extent with increasing power (the apparent increase in condensate size for trap size 13.7 m in Fig. 6 arises from an increased signal-to-noise ratio on the CCD). The profiles [Fig. 6(a)] remain the same independently of pump spin [Fig. 6(b): 4, 5], and of whether the condensate is in a spin-inverted region [Fig. 6(b): 2, 4, 6, 8] or in a hysteretic region [Fig. 6(b): 1, 3, 7].

In addition to there being no change in the spatial properties of the condensate, there is no evidence of higher-order modes in the polarization-resolved condensate spectrum (Fig. 7). As expected from the repulsive interactions between polaritons and the reservoir, the average condensate energy blueshifts with increasing pump power [Fig. 7(b)]. Unexpectedly, there can be a small energy splitting (less than one-third of the linewidth) between the two circular polarization components [Fig. 7(c)]. Three different regions can be highlighted. First, at low powers ($<P_{\rm inv}$) and large pump circularity, there is no observable energy difference between the two components [Fig. 7(e)]. Second, at lower pump circularities, and approximately at the transition between the U and the inverted regions, an energy difference ($\sim$20 μeV) appears. Here, the lower-energy mode is the one which is being pumped more strongly and has higher occupation, a very counterintuitive result when considering the repulsive nonlinearities. Third, for $P > P_{\rm inv}$, there is a small energy difference between the two components, with the component of the same handedness as the pump being at higher energy as expected. Note that this energy difference does not change depending on whether the condensate is spin inverted or not, indicating that the unusual regions U have some relation to the energy difference between the circularly polarized polariton modes, while the spin inversion does not.

V. THEORY AND SIMULATIONS

The exciton-polariton condensate behavior is captured by a spinor macroscopic wave function (order parameter)

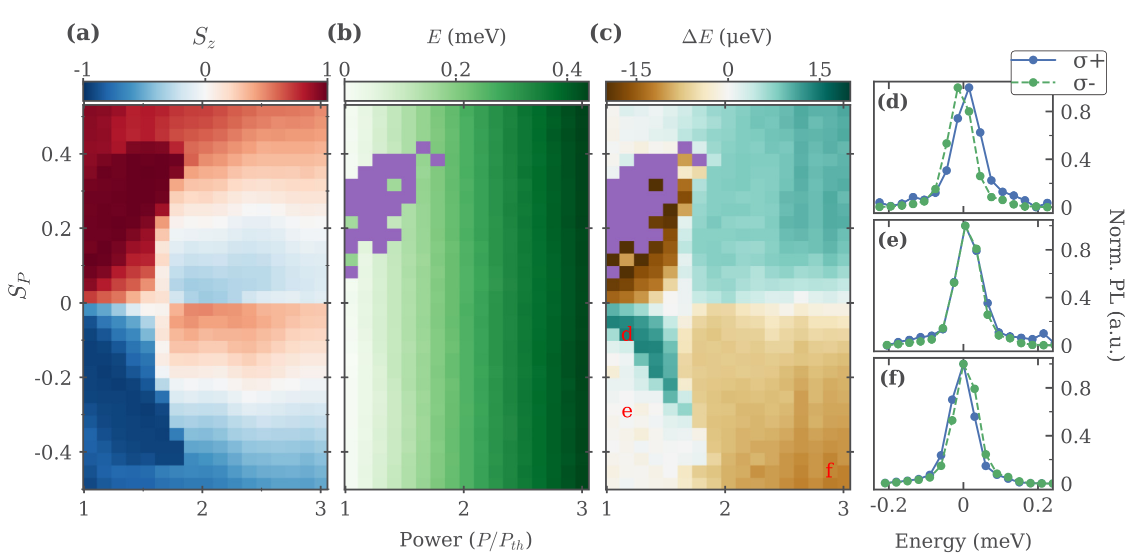

FIG. 7. (a), (b) Average (a) spin and (b) energy as a function of pump spin and power. Energy is measured relative to the polariton emission energy at threshold. Purple pixels correspond to spectra where one of the peaks was too small to resolve. (c) Energy difference between the two circularly polarized components. (d)–(f) Spectra for $S_P < 0$ showing (d) the counterintuitive splitting with the polarization of the same handedness as the pump at lower energy, (e) the synchronised case, and (f) the intuitive splitting with the polarization of the same handedness at higher energy.

$\Psi = (\psi_+, \psi_-)^T$ which is described by a non-Hermitian and nonlinear Schrödinger equation. Such driven-dissipative mean-field models have proven very successful at describing the phenomenology of polariton condensates [18]. Projecting the order parameter onto the ground state of the optically induced trap, the equations for the two components can be written [12,25–28]

$$\frac{d\psi_\pm}{dt} = \left[\frac{1}{2}(W_\pm - \Gamma_p) - \frac{i}{2}(\alpha_1|\psi_\pm|^2 + \alpha_2|\psi_\mp|^2 + V_\pm)\right]\psi_\pm - \frac{1}{2}(\gamma - i\,\varepsilon)\psi_\mp. \quad (1)$$

Here $W_\pm$ and $V_\pm$ are the particle harvest rates and blueshifts experienced by the two spin components of the wave function from a reservoir of uncondensed particles; Γ_p is the polariton lifetime; $\alpha_{1,2}$ are the same- and cross-spin polariton interaction parameters; and γ and ε are the dissipation and energy difference between the linearly polarized polariton modes. This rather general equation must be supplemented with definitions of the nonresonant feeding $W_\pm$ and blueshifts $V_\pm$. A very common approach is to consider an incoherent reservoir of n_+ spin-up and n_- spin-down excitons providing gain to the condensate through stimulated bosonic scattering and blueshifting the polariton energy levels through Coulomb interaction [33,34]:

$$W_\pm = R_s n_\pm + R_o\, n_\mp, \; V_\pm = g_1 n_\pm + g_2 n_\mp, \quad (2)$$

where $R_{s,o}$ are the same- and opposite-spin gain from the two spin-polarized reservoirs to the condensate and $g_{1,2}$ are the same- and cross-spin interaction constants. The final step is to then relate the nonresonant pump intensities ($P_\pm$) to the densities of these excitonic reservoirs by classical kinetic equations:

$$\frac{dn_\pm}{dt} = P_\pm - \Gamma_x n_\pm - (R_s|\psi_\pm|^2 + R_o|\psi_\mp|^2)n_\pm + \Gamma_s(n_\mp - n_\pm). \quad (3)$$

Here Γ_x is the exciton lifetime, and Γ_s denotes the spin-relaxation rate in the reservoir. This set of equations reduces to previously used models with different limiting values of the parameters: for $R_o = g_2 = \Gamma_s = 0$ one recovers the equations in Refs. [26–28], and for $R_s = R_o$, $P_+ = P_-$, $g_1 = g_2 = \Gamma_s = 0$, and adiabatically eliminating the reservoir dynamics one gets the equations in Refs. [12,25]. By numerically solving Eqs. (1)–(3) using 800-ns triangular pump pulses, the two main features of the trapped spinor condensate can be reproduced: spin inversion and spin bistability as observed in experiment (Fig. 8).

However, there are clear differences between numerical and experimental data, and an extensive scan of parameters fails to explain the new experimental results (Fig. 2). First, simulations show that the degree of circular polarization in the spin-inverted regions *increases* with pump spin, while the opposite trend is observed in experiment. Second, the simulations show no critical spin boundary (S_c) and the shape of the bright regions U is qualitatively different. Third, the width of the simulated hysteresis loops grows with S_P [Figs. 3(b) and 3(c)], but not in the experiment. Fourth, the energy splittings seen in experiment are not reproduced. Finally, while the

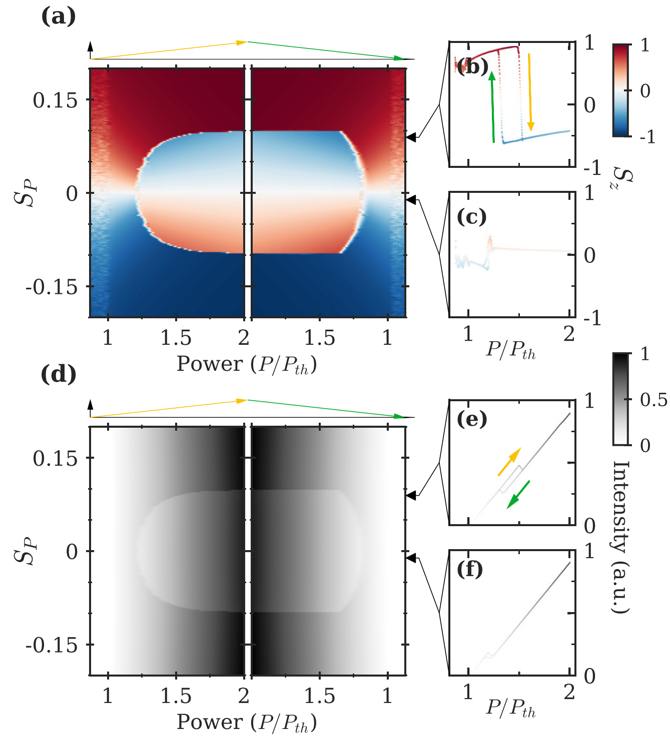

FIG. 8. (a), (d) Average (a) spin and (d) intensity as functions of power and pump spin, for increasing and decreasing power. (b), (c), (e), (f) Spin and intensity for (b), (e) $S_P = 0.06$ and (c), (f) -0.02. Parameter values for Eq. (1) are $\varepsilon = 0.06\,\mathrm{ps}^{-1}$, $\gamma = 0.05\varepsilon$, $\Gamma_\mathrm{p} = 0.1\,\mathrm{ps}^{-1}$, $\Gamma_x = 0.4\Gamma_p$, $\alpha_1 = 0.01\,\mathrm{ps}^{-1}$, $\alpha_2 = -0.1\alpha_1$, $R_s = 0.001\,\mathrm{ps}^{-1}$, $R_o = 0.6R_s$, $g_1 = 2\alpha_1$, $g_2 = -0.1g_1$, $\Gamma_s = \Gamma_x$.

experiment always displays spin bifurcation in the limit of linearly polarized pumping [Fig. 2(d)], the simulations do not. Therefore, while the previous two models (Refs. [26–28] and [12,25]) can separately explain parts of our results successfully, they fail to grasp the full picture.

It may appear that the stark differences between the model in Refs. [26–28] and the experimental data arise because of the absence of spatial dynamics in Eq. (1). An elliptically polarized excitation creates traps of different depths for each of the polariton spin components and consequently changes the wave function of each spin. This could then be a factor explaining why the model is unable to capture all the experimental features. To account for this, simulations accounting for the two-dimensional dynamics of the polariton wave function were performed using

$$\frac{d\psi_\pm}{dt} = -i\frac{\hbar\nabla^2\psi_\pm}{2m^*} + \left[\frac{1}{2}(W_\pm - \Gamma_p) - \frac{i}{2}(\alpha_1|\psi_\pm|^2 + \alpha_2|\psi_\mp|^2 + V_\pm)\right]\psi_\pm - \frac{1}{2}(\gamma - i\,\varepsilon)\psi_\mp. \quad (4)$$

The dispersion in Eq. (4) is taken to be parabolic because the condensate forms at small momenta on the lower polariton branch, m^* is the polariton mass, and $W_\pm$ and $V_\pm$. have the same form as in Eqs. (2) and (3). However, numerical integration of Eq. (4) show qualitatively similar results to Eq. (1): the trap ground state [Fig. 9(a)] initially has the same handedness as the pump and it reverses at a critical inversion threshold

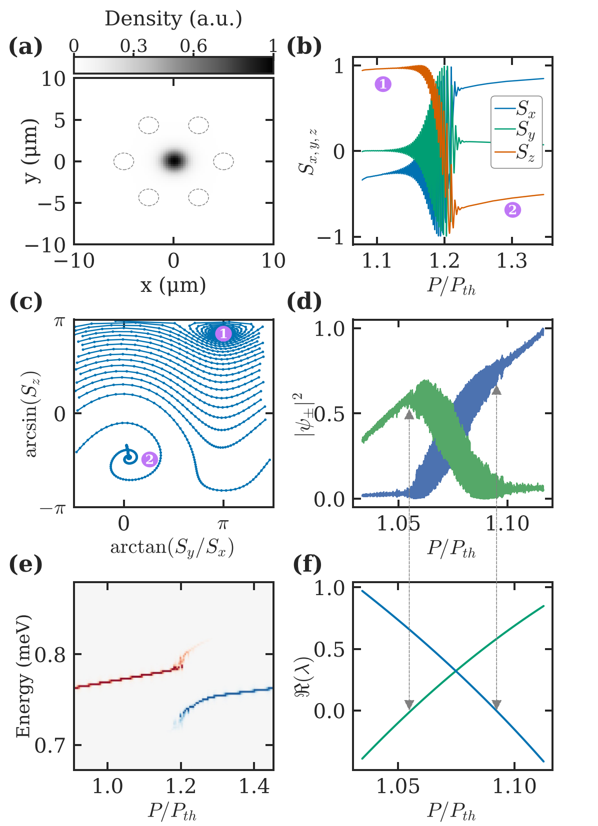

FIG. 9. (a) 2D simulations of an optically trapped condensate. Dashed circles indicate positions of the pump spots. (b) Normalized pseudospin values averaged over the center of the trap, for a ramped pump pulse. (c) Evolution of the pseudospin components on the surface of the Poincare sphere during the spin reversal. (d) Evolution of the spin components for a ramped pump pulse in the zero-dimensional model [Eq. (1)]. (e) Condensate energy as a function of pump power (same parameters as Fig. 8 with $S_p = 0.07$). Color indicates degree of circular polarization for each frequency. (f) Maximal Lyapunov exponents for the two fixed-point solutions. Each line corresponds to two degenerate exponents. Dashed vertical lines mark the regime where both fixed points are unstable. Parameter values for Eq. (4) are $\varepsilon = 0.03\,\text{ps}^{-1}$, $\gamma = 0$, $\gamma = 0$, $\Gamma_p = 0.1\,\text{ps}^{-1}$, $\Gamma_x = 0.7\Gamma_p$, $\alpha_1 = 0.06\,\text{ps}^{-1}\mu\text{m}^2$, $\alpha_2 = 0$, $R_s = 0.001\,\text{ps}^{-1}$, $R_o = 0.6R_s$, $g_1 = 3\alpha_1$, $g_2 = 0$, $\Gamma_s = 0$, $S_p = 0.05$, $m^* = 5.1 \times 10^{-5} m_e$. Note: nonzero α_2, γ, g_2, and Γ_s do not qualitatively change these results.

[Figs. 9(b) and 9(c)]. We have been unable to reproduce any of the other interesting features of the experiment.

Linear-stability analysis was performed on the two distinct fixed-point solutions of Eq. (1) with opposite dominant spin populations. To find these two fixed points of Eq. (1) corresponding to the solutions before and after the spin inversion a trust-region algorithm with the condition $i\partial_t \psi_\pm = \mu\psi_\pm$ and $\mu \in R$ is used. A standard Bogoliubov–de Gennes stability approach is then performed on the two fixed points to reveal that both become unstable for a range of pump powers. As the power is increased, two complex-conjugated Lyapunov exponents of the initial fixed-point solution cross zero, and the stable solution undergoes a Hopf bifurcation into limit cycle. As the power is further increased, a new stable fixed-point solution appears from other limit cycle oscillations (also by a Hopf bifurcation) and it becomes the stationary state of the system [Fig. 9(f)]. Therefore, the spin inversion is characterized by a limit cycle regime which separates the two stationary spin solutions as a function of pump power. This can be verified by numerically integrating Eq. (4) [Eq. (1)] in time and increasing the pump power slowly. The initial fixed-point state undergoes a Hopf bifurcation into a limit cycle at $P_0 \approx 1.14P_{\text{th}}$ ($1.05P_{\text{th}}$) and at higher powers exits the limit cycle via another Hopf bifurcation into the second fixed-point state $P_0 \approx 1.22P_{\text{th}}$ ($1.09P_{\text{th}}$) in Figs. 9(b) and 9(d), respectively. It is worth noting that the spins in the limit cycle regime are found to be energy comb synchronized in simulations, i.e., having the same set of equidistant energies in each spin component (see also Ref. [35] about this regime). The two main components of the frequency comb are shown in Fig. 9(e). The weights of each of the components are different for the two spins, which would result in an apparent energy splitting in the measured spectrum. However, the sign of this simulated splitting is the opposite to that in experiment: the higher energy mode is the one that is being pumped more strongly. Additionally, simulations show no energy splitting above the spin inversion threshold.

In the special case when $\gamma = \varepsilon = 0$, it straightforward to show that the handedness of the pump determines the handedness of the condensate at threshold. Setting nonlinearities to zero ($|\psi_\pm|^2 = 0$) and solving $\frac{dn_\pm}{dt} = 0$ one has

$$n_\pm = \frac{\Gamma_R P_\pm + \Gamma_s(P_+ + P_-)}{\Gamma_R(\Gamma_R + 2\Gamma_s)}. \tag{5}$$

Therefore if $P_+ > P_-$ then $n_+ > n_-$, and provided $R_s > R_o$ the reservoir which is being driven harder will populate its corresponding spin first. Note that, if $\gamma, \varepsilon \neq 0$, the polarization of the condensate at threshold will not be fully circularly polarized and it becomes linearly polarized as the pump becomes linear ($P_+ = P_-$). This is indicated by the whiter region in Fig. 8(a) at low power and low pump spin. Nevertheless, it always has the same handedness as the pump, which is in stark contrast with experiments [Figs. 4(c), 5(a), and 6(c)]. Experimental agreement could be achieved if the condition $R_s > R_o$ is relaxed, which is further discussed in the next section.

VI. DISCUSSION AND CONCLUSION

We have observed three distinct phenomena in optically trapped polariton condensates pumped with elliptically polarized nonresonant light. The first is the formation of condensates of opposite spin to that of the nonresonant pumping. The second is the hysteresis of both condensate spin and intensity as a function of pump power. The third is the collapse of the condensate spin above a critical pump ellipticity. These effects are linked to unusual (U) and inverted regions in the pump power vs pump polarization plane. The shape and extent of both these regions are strongly dependent on trap size and sample position, but nevertheless the universal trend is for larger traps to show spin inversion without hysteresis, while smaller traps can show hysteresis without spin inversion and even no spin inversion altogether.

Although the condensate spin and intensity depend strongly on pump spin and power, the spatial profile of the condensate itself is independent of these parameters and always condenses in the lowest mode of the trap, with no higher-energy modes visible in the spectrum (Sec. IV). However, for some parameters there is a small energy difference between the two circularly polarized condensate components. At low power, whether in the unusual or inverted region, the two components have the same energy. When transitioning from an unusual to inverted region by increasing the power, an energy difference appears, with the lower-energy component being that which has the same handedness as the pump and has a higher occupation. At high power, there is a smaller energy difference of the opposite sign, independently of whether the condensate is spin inverted or not.

Both spin inversion and hysteresis have been recently observed in similar semiconductor microcavities [26,27], and were both attributed to similar physical phenomena: an interplay of the reservoir nonlinearity with an energy splitting between linearly polarized polariton modes. Such simulations are unable to fully reproduce the pump spin dependence (Secs. II and V), explain the existence of a critical spin (S_c), capture the dependence on trap size and position (Sec. III), or capture the behavior of energy splittings between the circularly polarized modes. Future experiments measuring the hysteresis timescales [27] as a function of pump power, pump ellipticity, and trap size, as well as a measurement of all Stokes components, could provide further evidence for the adequacy or otherwise of these simulations. Additionally, both the spin-inversion and the hysteresis effects could be exploited in optically programmed polariton simulators [36]. In particular, nontrivial configurations of spins chains and lattices of nearly identical optically trapped condensates could be created by designing the ramping profile of each condensate.

These differences indicate that the current model of the excitonic reservoir is insufficient for the full description of optically trapped condensates. Accounting for the exciton reservoir spatial dynamics, including diffusion and spin precession due to TE-TM splitting in Eq. (3), could go some of the way in bridging the disagreement. For small trap sizes, the stronger overlap between the reservoir and the condensate would mean condensation always occurs in the same handedness as the pump, while for larger traps the spin of the reservoirs could rotate and drive the spin inversion. Alternatively, another possibility for the experiment-theory disagreement could stem from the simplistic reservoir-to-condensate scattering terms (R_s and R_o), which Eq. (2) assumed to be linear [33] but which could have more complicated dependencies on the reservoir density and trap size due to spin-dependent polariton relaxation [37]. Both of these extensions could mean that $W_\pm$ and $V_\pm$ could have complex and nonmonotonic dependences on the pump ellipticity and power. Finally, given that the system is driven with elliptically polarized light, spin pumping of the nuclear spins could be creating sufficiently large magnetic fields to split the polariton modes and affect the condensation [38]. This could explain the counterintuitive energy splitting as well as bistability, but the slow timescales ($>1s$) expected from nuclear spin reservoirs have not been seen. Our results thus demand further theoretical advances in developing an accurate microscopic description of the two-dimensional dynamics of spinor polariton condensate formation.

ACKNOWLEDGMENTS

We acknowledge Grants No. EPSRC EP/L027151/1 and No. ERC LINASS 320503, Leverhulme Trust Grant No. VP1-2013-011 and bilateral Greece-Russia ‘Polisimulator’ project co-financed by Greece and the EU Regional Development Fund. H.S. acknowledges support by the Research Fund of the University of Iceland, The Icelandic Research Fund, Grant No. 163082-051. The work of IAS on theoretical analysis of the discovered effects was supported by the Ministry of Education and Science of Russian Federation, Projects 14.Y26.31.0015 and 3.2614.2017/4.6. Y.G.R. acknowledges support from CONACYT (Mexico) under Grant No. 251808. The work of PS on structure growth and characterization was supported by Russian Science Foundation, Grant No. 19-72-20120.

[1] S. Strogatz, *Nonlinear Dynamics and Chaos* (CRC, Boca Raton, FL, 2000).

[2] H. M. Gibbs, *Optical Bistability: Controlling Light With Light* (Academic, New York, 1985).

[3] A. Baas, J. P. Karr, H. Eleuch, and E. Giacobino, Optical bistability in semiconductor microcavities, Phys. Rev. A **69**, 023809 (2004).

[4] N. A. Gippius, I. A. Shelykh, D. D. Solnyshkov, S. S. Gavrilov, Y. G. Rubo, A. V. Kavokin, S. G. Tikhodeev, and G. Malpuech, Polarization Multistability of Cavity Polaritons, Phys. Rev. Lett. **98**, 236401 (2007).

[5] T. K. Paraïso, M. Wouters, Y. Léger, F. Morier-Genoud, and B. Deveaud-Plédran, Multistability of a coherent spin ensemble in a semiconductor microcavity, Nat. Mater. **9**, 655 (2010).

[6] R. Cerna, Y. Léger, T. K. Paraïso, M. Wouters, F. Morier-Genoud, M. T. Portella-Oberli, and B. Deveaud, Ultrafast tristable spin memory of a coherent polariton gas, Nat. Commun. **4**, 2008 (2013).

[7] T. C. H. Liew, A. V. Kavokin, and I. A. Shelykh, Optical Circuits Based on Polariton Neurons in Semiconductor Microcavities, Phys. Rev. Lett. **101**, 016402 (2008).

[8] T. Espinosa-Ortega and T. C. H. Liew, Complete architecture of integrated photonic circuits based on and and not logic gates of exciton polaritons in semiconductor microcavities, Phys. Rev. B **87**, 195305 (2013).

[9] A. Amo, T. C. H. Liew, C. Adrados, R. Houdre, E. Giacobino, A. V. Kavokin, and A. Bramati, Exciton-polariton spin switches, Nat. Photon **4**, 361 (2010).

[10] D. Bajoni, E. Semenova, A. Lemaître, S. Bouchoule, E. Wertz, P. Senellart, S. Barbay, R. Kuszelewicz, and J. Bloch, Optical Bistability in a GaAs-Based Polariton Diode, Phys. Rev. Lett. **101**, 266402 (2008).

[11] M. Amthor, T. C. H. Liew, C. Metzger, S. Brodbeck, L. Worschech, M. Kamp, I. A. Shelykh, A. V. Kavokin, C. Schneider, and S. Höfling, Optical Bistability in Electrically

Driven Polariton Condensates, Phys. Rev. B **91**, 081404(R) (2015).

[12] A. Dreismann, H. Ohadi, Y. del Valle-Inclan Redondo, R. Balili, Y. G. Rubo, S. I. Tsintzos, G. Deligeorgis, Z. Hatzopoulos, P. G. Savvidis, and J. J. Baumberg, A Sub-femtojoule electrical spin-switch based on optically trapped polariton condensates, Nat. Mater. **15**, 1074 (2016).

[13] O. Kyriienko, E. A. Ostrovskaya, O. A. Egorov, I. A. Shelykh, and T. C. H. Liew, Bistability in microcavities with incoherent optical or electrical excitation, Phys. Rev. B **90**, 125407 (2014).

[14] D. V. Karpov, I. G. Savenko, H. Flayac, and N. N. Rosanov, Dissipative soliton protocols in semiconductor microcavities at finite temperatures, Phys. Rev. B **92**, 075305 (2015).

[15] E. Z. Tan, H. Sigurdsson, and T. C. H. Liew, Parity bifurcations in trapped multistable phase locked exciton-polariton condensates, Phys. Rev. B **97**, 075305 (2018).

[16] J. Kasprzak, D. D. Solnyshkov, R. André, L. S. Dang, and G. Malpuech, Formation of an Exciton Polariton Condensate: Thermodynamic Versus Kinetic Regimes, Phys. Rev. Lett. **101**, 146404 (2008).

[17] T. Byrnes, N. Y. Kim, and Y. Yamamoto, Exciton-polariton condensates, Nat. Phys. **10**, 803 (2014).

[18] I. Carusotto and C. Ciuti, Quantum fluids of light, Rev. Mod. Phys. **85**, 299 (2013).

[19] F. Manni, K. G. Lagoudakis, T. C. H. Liew, R. André, and B. Deveaud-Plédran, Spontaneous Pattern Formation in a Polariton Condensate, Phys. Rev. Lett. **107**, 106401 (2011).

[20] E. Wertz, L. Ferrier, D. D. Solnyshkov, R. Johne, D. Sanvitto, A. Lemaître, I. Sagnes, R. Grousson, A. V. Kavokin, P. Senellart, G. Malpuech, and J. Bloch, Spontaneous formation and optical manipulation of extended polariton condensates, Nat. Phys. **6**, 860 (2010).

[21] R. Dall, M. D. Fraser, A. S. Desyatnikov, G. Li, S. Brodbeck, M. Kamp, C. Schneider, S. Höfling, and E. A. Ostrovskaya, Creation of Orbital Angular Momentum States with Chiral Polaritonic Lenses, Phys. Rev. Lett. **113**, 200404 (2014).

[22] A. Askitopoulos, H. Ohadi, A. V. Kavokin, Z. Hatzopoulos, P. G. Savvidis, and P. G. Lagoudakis, Polariton condensation in an optically induced two-dimensional potential, Phys. Rev. B **88**, 041308(R) (2013).

[23] P. Cristofolini, A. Dreismann, G. Christmann, G. Franchetti, N. G. Berloff, P. Tsotsis, Z. Hatzopoulos, P. G. Savvidis, and J. J. Baumberg, Optical Superfluid Phase Transitions and Trapping of Polariton Condensates, Phys. Rev. Lett. **110**, 186403 (2013).

[24] A. Askitopoulos, T. C. H. Liew, H. Ohadi, Z. Hatzopoulos, P. G. Savvidis, and P. G. Lagoudakis, Robust platform for engineering pure-quantum-state transitions in polariton condensates, Phys. Rev. B **92**, 035305 (2015).

[25] H. Ohadi, A. Dreismann, Y. G. Rubo, F. Pinsker, Y. del Valle-Inclan Redondo, S. I. Tsintzos, Z. Hatzopoulos, P. G. Savvidis, and J. J. Baumberg, Spontaneous Spin Bifurcations and Ferromagnetic Phase Transitions in a Spinor Exciton-Polariton Condensate, Phys. Rev. X **5**, 031002 (2015).

[26] A. Askitopoulos, K. Kalinin, T. C. H. Liew, P. Cilibrizzi, Z. Hatzopoulos, P. G. Savvidis, N. G. Berloff, and P. G. Lagoudakis, Nonresonant optical control of a spinor polariton condensate, Phys. Rev. B **93**, 205307 (2016).

[27] L. Pickup, K. Kalinin, A. Askitopoulos, Z. Hatzopoulos, P. G. Savvidis, N. G. Berloff, and P. G. Lagoudakis, Optical Bistability Under Non-Resonant Excitation in Spinor Polariton Condensates, Phys. Rev. Lett. **120**, 225301 (2018).

[28] G. Li, T. C. H. Liew, O. A. Egorov, and E. A. Ostrovskaya, Incoherent excitation and switching of spin states in exciton-polariton condensates, Phys. Rev. B **92**, 064304 (2015).

[29] P. Tsotsis, P. S. Eldridge, T. Gao, S. I. Tsintzos, Z. Hatzopoulos, and P. G. Savvidis, Lasing threshold doubling at the crossover from strong to weak coupling regime in GaAs microcavity, New J. Phys. **14**, 023060 (2012).

[30] M. Pasienski and B. DeMarco, A High-accuracy algorithm for designing arbitrary holographic atom, Traps Opt. Express **16**, 2176 (2008).

[31] Y. del V.-I. Redondo, H. Ohadi, Y. G. Rubo, O. Beer, A. J. Ramsay, S. I. Tsintzos, Z. Hatzopoulos, P. G. Savvidis, and J. J. Baumberg, Stochastic spin flips in polariton condensates: Nonlinear tuning from GHz to sub-Hz, New J. Phys. **20**, 075008 (2018).

[32] Y. Sun, Y. Yoon, S. Khan, L. Ge, M. Steger, L. N. Pfeiffer, K. West, H. E. Türeci, D. W. Snoke, and K. A. Nelson, Stable switching among high-order modes in polariton condensates, Phys. Rev. B **97**, 045303 (2018).

[33] M. Wouters, I. Carusotto, and C. Ciuti, Spatial and spectral shape of inhomogeneous nonequilibrium exciton-polariton condensates, Phys. Rev. B **77**, 115340 (2008).

[34] M. Wouters and I. Carusotto, Excitations in a Nonequilibrium Bose-Einstein Condensate of Exciton Polaritons, Phys. Rev. Lett. **99**, 140402 (2007).

[35] K. Rayanov, B. L. Altshuler, Y. G. Rubo, and S. Flach, Frequency Combs with Weakly Lasing Exciton-Polariton Condensates, Phys. Rev. Lett. **114**, 193901 (2015).

[36] H. Ohadi, A. J. Ramsay, H. Sigurdsson, Y. del Valle-Inclan Redondo, S. I. Tsintzos, Z. Hatzopoulos, T. C. H. Liew, I. A. Shelykh, Y. G. Rubo, P. G. Savvidis, and J. J. Baumberg, Spin Order and Phase Transitions in Chains of Polariton Condensates, Phys. Rev. Lett. **119**, 067401 (2017).

[37] G. Roumpos, C.-W. Lai, T. C. H. Liew, Y. G. Rubo, A. V. Kavokin, and Y. Yamamoto, Signature of the microcavity exciton-polariton relaxation mechanism in the polarization of emitted light, Phys. Rev. B **79**, 195310 (2009).

[38] T. C. H. Liew and V. Savona, Optically Erasing Disorder in Semiconductor Microcavities with Dynamic Nuclear Polarization, Phys. Rev. Lett. **106**, 146404 (2011).